AGU PUBLICATIONS

JGR

Journal of Geophysical Research: Space Physics

RESEARCH ARTICLE
10.1002/2015JA021143

Key Points:
- Developed global MHD model of Mercury's magnetosphere with coupled interior
- The global model is able to self-consistently model induction effect at the core
- Induction effect is shown to have significant effects on the global interaction

Correspondence to:
X. Jia,
xzjia@umich.edu

Citation:
Jia, X., J. A. Slavin, T. I. Gombosi, L. K. S. Daldorff, G. Toth, and B. van der Holst (2015), Global MHD simulations of Mercury's magnetosphere with coupled planetary interior: Induction effect of the planetary conducting core on the global interaction, *J. Geophys. Res. Space Physics*, *120*, 4763–4775, doi:10.1002/2015JA021143.

Received 19 FEB 2015
Accepted 27 MAY 2015
Accepted article online 1 Jun 2015
Published online 23 JUN 2015

Global MHD simulations of Mercury's magnetosphere with coupled planetary interior: Induction effect of the planetary conducting core on the global interaction

Xianzhe Jia[1], James A. Slavin[1], Tamas I. Gombosi[1], Lars K. S. Daldorff[1], Gabor Toth[1], and Bart van der Holst[1]

[1]Department of Atmospheric, Oceanic and Space Sciences, University of Michigan, Ann Arbor, Michigan, USA

Abstract Mercury's comparatively weak intrinsic magnetic field and its close proximity to the Sun lead to a magnetosphere that undergoes more direct space-weathering interactions than other planets. A unique aspect of Mercury's interaction system arises from the large ratio of the scale of the planet to the scale of the magnetosphere and the presence of a large-size core composed of highly conducting material. Consequently, there is strong feedback between the planetary interior and the magnetosphere, especially under conditions of strong external forcing. Understanding the coupled solar wind-magnetosphere-interior interaction at Mercury requires not only analysis of observations but also a modeling framework that is both comprehensive and inclusive. We have developed a new global MHD model for Mercury in which the planetary interior is modeled as layers of different electrical conductivities that electromagnetically couple to the surrounding plasma environment. This new modeling capability allows us to characterize the dynamical response of Mercury to time-varying external conditions in a self-consistent manner. Comparison of our model results with observations by the MErcury Surface, Space ENvironment, GEochemistry, and Ranging (MESSENGER) spacecraft shows that the model provides a reasonably good representation of the global magnetosphere. To demonstrate the capability to model induction effects, we have performed idealized simulations in which Mercury's magnetosphere is impacted by a solar wind pressure enhancement. Our results show that due to the induction effect, Mercury's core exerts strong global influences on the way Mercury responds to changes in the external environment, including modifying the global magnetospheric structure and affecting the extent to which the solar wind directly impacts the surface. The global MHD model presented here represents a crucial step toward establishing a modeling framework that enables self-consistent characterization of Mercury's tightly coupled planetary interior-magnetosphere system.

1. Introduction

At Mercury, the weak planetary magnetic field and its close proximity to the Sun give rise to a magnetosphere, a large fraction of which is occupied by the planet itself. Lack of an appreciable atmosphere or an ionosphere leads to more direct space weathering of the surface at Mercury than at other terrestrial planets. The recent measurements acquired by MESSENGER provide interesting new data about Mercury's magnetosphere, including first in situ measurements of planetary heavy ions in the magnetosphere [e.g., *Zurbuchen et al.*, 2008, 2011] and observations of magnetospheric dynamics dominated by effects of magnetic reconnection [*Slavin et al.*, 2009; *Dibraccio et al.*, 2013], such as frequent flux transfer events on the magnetopause [e.g., *Slavin et al.*, 2012; *Imber et al.*, 2014], plasmoids [*Dibraccio et al.*, 2014], and dipolarization fronts [*Sundberg et al.*, 2012] as well as strong loading/unloading events in the magnetotail [*Slavin et al.*, 2010].

A unique aspect of Mercury's interaction system that distinguishes itself from all the other planetary magnetospheres relates to the presence of a large-size core with a radius of $\sim 0.8\,R_M$ ($R_M = 2440$ km is Mercury's radius) composed of highly conducting material [e.g., *Smith et al.*, 2012; *Hauck et al.*, 2013] and the large ratio of the scale of the planet to the scale of the tiny magnetosphere. Because the external current systems arising from the magnetospheric interaction lie very close to the planet, the strength of the external field perturbations can be a significant fraction of Mercury's weak intrinsic field near the surface, a situation markedly different from that at Earth and other magnetized planets [*Glassmeier et al.*, 2007a]. In response to time-varying solar wind

conditions, Mercury's magnetosphere changes its size and the dayside magnetopause and the tail current sheet change their positions with respect to the planet. The motion of the magnetopause and its associated current systems leads to temporal variations of the external magnetic field perturbations near the planetary surface and in the planet's interior, which can induce strong electric currents in regions of high electrical conductivity. These electric currents in turn produce induced magnetic fields that can affect remote regions away from the conducting region.

The induced magnetic field arising from the planetary interior has been suggested to have profound effects on the global magnetospheric configuration [*Hood and Schubert*, 1979; *Suess and Goldstein*, 1979; *Slavin et al.*, 2014] and potentially on the dynamo action through which the internal field is generated [*Glassmeier et al.*, 2007b; *Heyner et al.*, 2011]. For instance, when Mercury is impacted by solar wind pressure enhancement, the induced magnetic field generated at the planetary core can add to the intrinsic magnetic field, thereby preventing the dayside magnetosphere from collapsing onto the planet. Such a feedback interaction tends to temporarily limit the direct access of solar wind particles to the surface of the planet. It is clear that the electromagnetic coupling between the planetary interior and the magnetosphere is a crucial element of Mercury's interaction system. Understanding this feedback is key to understanding how Mercury's space environment responds to the external forcing, such as the coronal mass ejection (CME) impacts recently observed at Mercury [*Slavin et al.*, 2014].

Global simulation models, including both magnetohydrodynamic (MHD) and hybrid models, have been developed to understand the roles of the solar wind and planetary ions in determining the global structure and driving dynamics of Mercury's magnetosphere. These global models provide global context for interpreting measurements obtained in various parts of the system, thereby extending our knowledge of Mercury's magnetospheric environment beyond that available from localized spacecraft observations. In this paper, we present a newly developed Mercury global MHD model that electromagnetically couples the planetary interior with its surrounding magnetosphere (section 2). We demonstrate that the coupling capability implemented in this model allows us to self-consistently characterize the dynamical response of the Mercury system to time-varying external conditions, thereby enabling quantitative characterization of the induction effect arising from the planet's conducting core on the global magnetosphere.

2. Global MHD Model With Coupled Planetary Interior

We simulate Mercury's interaction with the solar wind by using the global MHD model, BATSRUS (Block Adaptive Tree Solar wind Roe-type Upwind Scheme) [*Powell et al.*, 1999; *Gombosi et al.*, 2002], which is the global magnetosphere component of the Space Weather Modeling Framework (SWMF) developed to simulate the space environments around a variety of planetary bodies [*Tóth et al.*, 2012]. We note that although MHD does not treat kinetic aspects of the plasma system (e.g., energy-dependent drifts and finite gyroradius effects), an MHD model can provide insight into large-scale behavior of the magnetospheric system. Since our focus here is global structure of Mercury's coupled solar wind-magnetosphere-interior system, MHD simulation is an appropriate tool for our investigation.

BATSRUS has been previously applied by *Kabin et al.* [2000, 2008] to Mercury to study the large-scale structure of Mercury's magnetosphere and its variation in response to different solar wind conditions. However, Mercury's interior properties, especially the high conductivity associated with the planetary core, were not taken into account in the previous simulations. Our new model is developed specifically to include the planetary interior such that the feedback between the magnetosphere and the core can be directly modeled in a self-consistent manner. Below we present a summary of the BATSRUS model basics and its adaption to Mercury, followed by a description of the approach used to couple the planetary interior in BATSRUS.

2.1. Model Basics

The BATSRUS code solves the governing equations of magnetohydrodynamics (conservation of mass, momentum, and energy equations together with Faraday's law) with a conservative finite-volume method [*Powell et al.*, 1999; *Gombosi et al.*, 2002]. It uses a limited reconstruction that ensures second-order accuracy away from discontinuities while providing the stability that ensures nonoscillatory solutions. BATSRUS allows the use of generalized curvilinear coordinates, which provide a smooth mapping from a logically Cartesian grid to an arbitrary curvilinear grid, including spherical, cylindrical, and toroidal grids [*Tóth et al.*, 2012]. For the Mercury simulations presented here, a nonuniform spherical grid is employed to enable

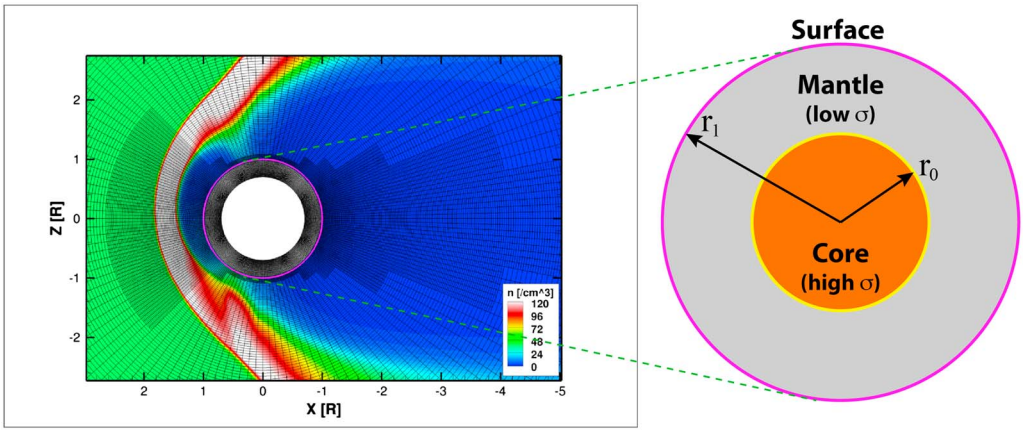

Figure 1. Simulation setup of the MHD model that electromagnetically couples the interior of Mercury with the external plasma environment. (left) A typical spherical grid used in the Mercury simulations viewed in the noon-midnight meridian (*XZ* plane in the MSO coordinates). Color contours of plasma density extracted from the simulation are plotted to delineate the global configuration of Mercury's magnetosphere. High-resolution grids are placed near the planet, the dayside magnetosphere, and the low-latitude magnetotail. (right) A schematic illustrating how Mercury's interior is modeled in the present simulation. The magenta circle corresponds to the surface, and the yellow circle represents the core-mantle boundary.

accurate prescription of boundary conditions near the planet and also to ensure high resolution in regions of interest. Figure 1 shows a typical grid distribution in a meridional cut through a portion of the 3-D spherical mesh used in our model. Owing to the adaptive mesh refinement capability of BATSRUS, the spherical grid used here provides fine resolution in the near-planet region, around the magnetospheric boundaries (such as the bow shock and magnetopause) and the equatorial tail current sheet. The grid resolution near the planet reaches ~ 0.008 R_M (~ 20 km) and increases to ~ 0.02 R_M (~ 50 km) near 2 R_M.

Simulation results shown in this paper are presented in a Mercury-centered Cartesian coordinate system called the Mercury solar orbital (MSO) coordinates, where $\hat{X}$ is along the Mercury-Sun line, $\hat{Z}$ is parallel to Mercury's rotation axis, and $\hat{Y}$ completes a right-handed system with positive pointing in the direction opposite to the orbital motion. We set a rectangular computational domain covering the region $-64R_M < X_{\mathrm{MSO}} < 24R_M$, $-32R_M < Y_{\mathrm{MSO}}, Z_{\mathrm{MSO}} < 32R_M$. To include the planetary interior in the simulation, the inner boundary of the global MHD model is placed below the planetary surface as will be described below.

2.2. Approach to Coupling Planetary Interior

A number of global simulation models have been applied to Mercury, including single-fluid MHD [*Kabin et al.*, 2000; *Ip and Kopp*, 2002], multifluid MHD [*Kidder et al.*, 2008; *Benna et al.*, 2010], and hybrid [*Kallio and Janhunen*, 2003; *Janhunen and Kallio*, 2004; *Trávníček et al.*, 2007; *Wang et al.*, 2010; *Müller et al.*, 2012; *Richer et al.*, 2012] simulations. However, all of these Mercury global models, except for the hybrid models of *Janhunen and Kallio* [2004] and *Müller et al.* [2012], which will be discussed later, did not include the planetary interior as part of the simulation domain, and, instead, they treated the planet as a purely absorbing obstacle without taking into account the electrical properties of the planetary interior. To model the induction effect arising from the core, it is essential to include the interior region explicitly in global models. To do so, we have implemented in BATSRUS a new capability of electromagnetically coupling a planetary body with the ambient space plasma following the approach that was applied previously to Jupiter's moons, Io [*Linker et al.*, 1998; *Khurana et al.*, 2011] and Ganymede [*Jia et al.*, 2008, 2009, 2010], where this method has been demonstrated to provide an appropriate way for modeling plasma interaction with a planetary body of finite conductivity.

The basic concept of the approach to coupling Mercury's interior with the space environment is illustrated in Figure 1. As far as the magnetospheric interaction and the resultant large-scale current systems are concerned, the most important property of the planetary interior is the electrical conductivity as it determines the way in which the magnetic field diffuses through the body. To take this into account, we use the resistive MHD version of BATSRUS that allows us to explicitly specify the distribution of resistivity (or the inverse of conductivity), which is then used in the generalized Ohm's law and the magnetic induction equation to advance the magnetic field. The full set of the resistive MHD equations, i.e, continuity, momentum, energy, and

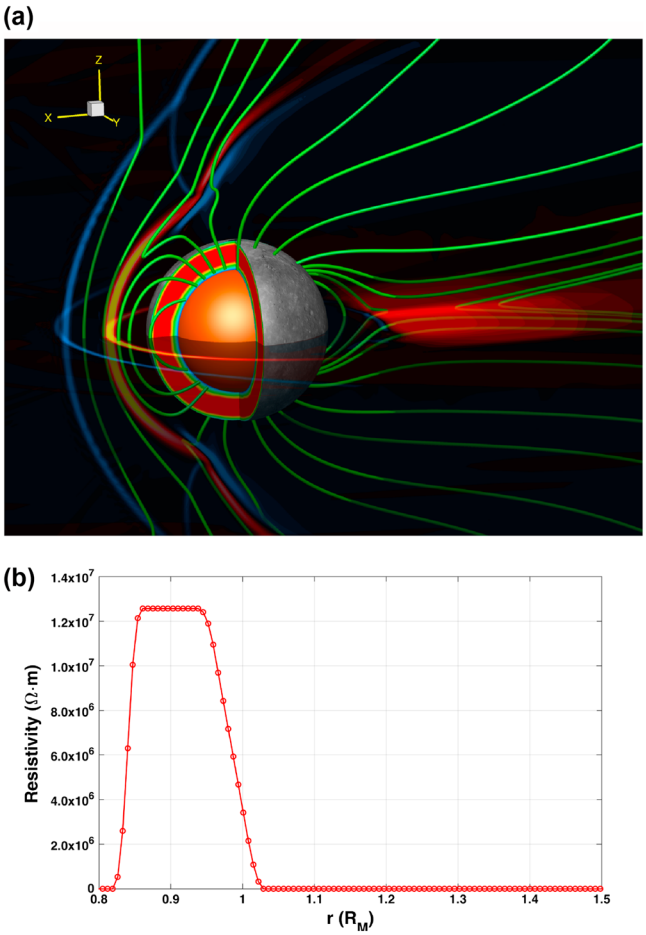

Figure 2. (a) A 3-D view of Mercury's magnetosphere extracted from the global MHD model with coupled planetary interior. Green traces show sampled magnetic field lines, while colors in the magnetosphere denote the current density J_y with red/yellow representing positive J_y and blue representing negative J_y. The simulation inner boundary is located at $r = 0.8R_M$ (shown by the orange sphere), corresponding to the outer boundary of Mercury's highly conducting core. The region between Mercury's surface and the conducting core is color coded according to the resistivity values used in the model, with red meaning high resistivity and blue/green meaning low resistivity. (b) Radial profile of the resistivity used in the model.

induction equations, are solved throughout the entire simulation domain that extends from the outer layer of the core ($r = r_0 < 1R_M$) to the simulation outer boundary, which is typically placed at distances of $> 20\ R_M$ from the planet. Inside the planet ($r < 1\ R_M$) where plasma convection can be neglected, we set the plasma velocity to zero, thereby making the induction equation into a pure diffusion equation for the magnetic field ($\vec{B}$): $\frac{\partial \vec{B}}{\partial t} = -\frac{1}{\mu_0}\nabla \times (\eta \nabla \times \vec{B})$, where μ_0 is the permeability of vacuum and η denotes the resistivity (which is the inverse of the electrical conductivity, σ). Boundary conditions for the magnetic field need to be set at the core boundary ($r = r_0$), where the magnetic flux corresponding to Mercury's internal dipole, which has an equatorial surface strength of 195 nT and whose center is offset northward by 0.2 R_M from the equator [*Anderson et al.*, 2011], is prescribed and fixed in time. In order to efficiently solve the magnetic diffusion equation inside the planetary body, we use a semi-implicit time-integration scheme which allows the code to handle the set of MHD equations with such stiff source terms as those involving spatial derivatives of the resistivity [*Tóth et al.*, 2012]. At the surface, boundary conditions are set for the plasma parameters in a way such that the planet acts approximately as an inert body to the incoming plasma. If the plasma flow in the neighboring cell above the surface has an inflow component, floating conditions are applied to both the plasma density and pressure. If the plasma flow above the surface has an outflow component, then the radial velocity at the boundary is set to zero, while the plasma density and pressure are fixed at small constant values (1 cm^{-3} and 0.001 nPa, respectively), consistent with the fact that the planet itself is not a significant source of plasma.

In principle, the planetary interior in this model can have an arbitrary spatial distribution of electrical conductivities. For the case of Mercury, we have assumed a simplified model in which the interior is divided into two parts: the inner layer ($r < r_0 = 0.8R_M$) with high conductivity corresponding to the conducting core and the outer layer ($r_0 = 0.8R_M < r < r_1 = 1.0R_M$) with low conductivity representing the mantle. Our choice of the electrical conductivities for the mantle and the core is guided mainly by inferences from geophysical measurements and interior models [e.g., *Siegfried and Solomon*, 1974; *Smith et al.*, 2012; *Hauck et al.*, 2013]. Figure 2 shows the spatial distribution of the resistivity used in the current model. The entire resistivity profile is spherically symmetric, depending only on radial distance, and is fixed throughout the run. For the mantle (from the surface to $\sim$ 350 km depth) we set an average resistivity of $\sim 10^7 \Omega$ m (or equivalently a conductivity of $\sim 10^{-7}$ S/m). The resistivity then decreases linearly to $10^{-5}\Omega$ m (or a conductivity of 10^5 S/m) at the outer boundary of the core. As will be shown below, first results from our simulations demonstrate that this approach works reasonably well and the model is suitable for studying the solar wind interaction with the planetary interior and the magnetosphere as a tightly coupled system.

3. Simulation Results

We have benchmarked and tested the new MHD model by running simulations with various upstream conditions including both idealized input and those pertinent to MESSENGER observations. Here we present model results from a simulation for MESSENGER's second flyby of Mercury (M2) during which the interplanetary magnetic field (IMF) has a steady southward component. Due to lack of measurements of the upstream solar wind during this flyby, we adopt typical values of the solar wind bulk properties at Mercury's orbit [e.g., *Baker et al.*, 2013]. In particular, we use $n_{sw} = 40$ cm^{-3}, $T_{sw} = 15$ eV, and $[V_x, V_y, V_z] = [-400, 50, 0]$ km/s for the upstream plasma density, temperature, and velocity, respectively. The resulting solar wind dynamic pressure is $\sim$ 10.8 nPa. The solar wind flow velocity used contains a finite y component (V_y) in the MSO coordinates in order to take into account Mercury's orbital motion relative to the radially moving solar wind flow from the Sun. The IMF is set to be $[B_x, B_y, B_z] = [-15.2, 8.4, -8.5]$ nT according to the average values of the magnetometer measurements when MESSENGER was embedded in the solar wind [*Slavin et al.*, 2009].

3.1. Global Magnetospheric Configuration and Comparison With MESSENGER Observations

We first use the M2 flyby simulation results to illustrate the large-scale configuration of the modeled magnetosphere. Figure 3a shows the model results in the noon-midnight meridional plane, where color contours of plasma pressure along with projections of sampled magnetic field lines are plotted to delineate the magnetospheric configuration. One notable feature of the modeled magnetosphere is the strong asymmetries with respect to the planetary equatorial plane, which arise due to the northward offset of the planetary dipole as well as the presence of a strong negative IMF B_x. Some general features of the modeled magnetosphere can be compared directly with MESSENGER observations, such as the location and shape of various important boundaries. For the upstream conditions used here, the magnetopause and bow shock standoff distances in our model are about 1.5 R_M and 1.9 R_M, respectively, in accordance with MESSENGER observations of the magnetosphere under average upstream conditions [*Winslow et al.*, 2013]. Also plotted in Figure 3a is the modeled magnetopause boundary (magenta line) identified based on the total current density. For comparison, the empirical magnetopause model of *Winslow et al.* [2013] constructed based on MESSENGER data is also plotted. As can be seen, the overall shape of the magnetopause boundary in our model is in general agreement with the data-based model. The nightside X-line in the model is located at about 2 R_M from the planet's center, also in agreement with the survey results obtained by *Dibraccio et al.* [2014] using MESSENGER orbital data. Also evident in this figure is a pair of cusps located at $\sim 70^\circ$ northern latitude and $\sim 65^\circ$ southern latitude where the plasma pressure is enhanced with peak values reaching $\sim$ 5 nPa, consistent with the average cusp properties seen in MESSENGER observations [*Winslow et al.*, 2012; *Raines et al.*, 2014].

Figure 3b shows a YZ cut at $X = 0$ through the simulation in which the color contours represent the x component of the modeled plasma flow velocity (V_x) and the lines with arrows are sampled field lines. Key regions of the interaction can be readily identified based on the V_x contours. The transition from the ambient solar wind speed of $\sim$ 400 km/s to $\sim$ 200 km/s, which is characteristic of the magnetosheath flow at the terminator, marks the boundary of the bow shock, whereas further inward the transition from the sheath flows to convection flows with much smaller speeds ($< \sim$100 km/s) marks the magnetopause boundary. Inside the magnetosphere, flows with negative V_x at high latitudes are the cross-polar cap flows moving in the antisunward direction, while the flows with positive V_x at low latitudes are those return flows convecting from the

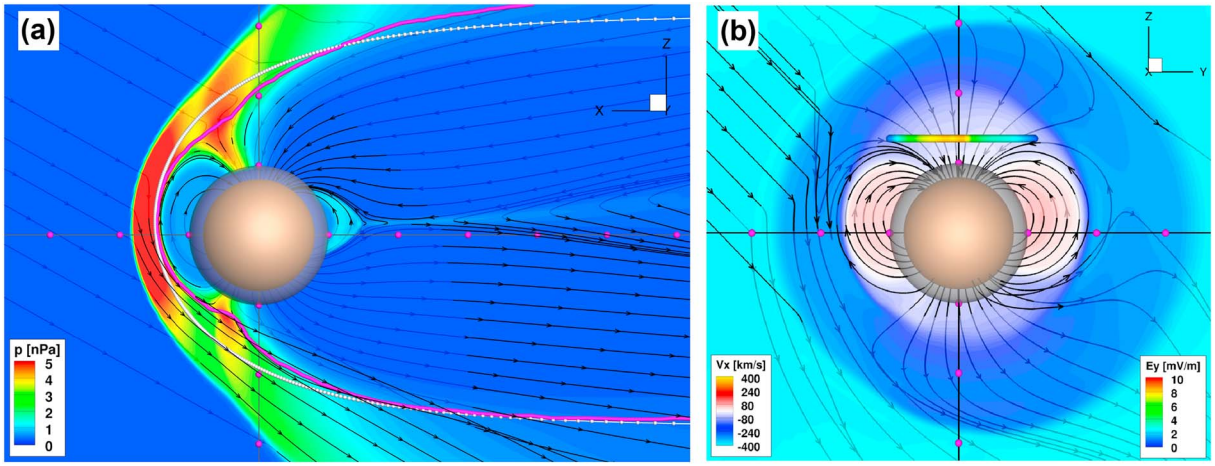

Figure 3. Cuts through the simulation of the MESSENGER M2 flyby. (a) *XZ* cut at $Y = 0$ (noon-midnight meridian) with color contours of plasma thermal pressure. The thick magenta line shows the modeled magnetopause boundary identified based on the current density, while the white dotted line represents the data-based empirical magnetopause model of *Winslow et al.* [2013], which has been scaled for the solar wind pressure of 10.8 nPa and shifted northward by 0.2 R_M. (b) *YZ* cut at $X = 0$ (terminator plane) with color contours of the *x* component of the flow velocity (V_x). The horizontal line at $Z = 1.3R_M$ is color coded by the *y* component of the convectional electric field (E_y), from which the cross-polar cap potential is calculated. In both panels, the black lines with arrows show the projection of sampled magnetic field lines onto the cut planes. The orange sphere has a radius of 0.8 R_M corresponding to the inner boundary of the simulation, while the grey sphere with a radius of 1 R_M represents the surface of the planet. Magenta balls are marked off every 1 R_M along the axes.

night side to the day side. From the results shown in Figure 3b we can obtain the cross-polar cap potential in the model, which provides a global measure of the strength of the coupling between the magnetosphere and the solar wind. We calculate the total potential drop by integrating the dawn-to-dusk component of the convectional electric field along a horizontal line (at $Z = 1.3\ R_M$) that spans the entire polar cap within which field lines are all connected to the solar wind. The resultant potential drop in our model is about 25 kV, in reasonable agreement with the 30 kV estimated by *Slavin et al.* [2009] for this flyby based on MESSENGER magnetic field observation.

As a further validation of the model, we compare the magnetic field extracted from the M2 flyby simulation along the MESSENGER trajectory with the observed magnetic field. Figure 4 shows the simulated magnetic field geometry along the flyby trajectory as well as the global magnetospheric structure as indicated by the color contours of plasma density. The simulated field strength along the trajectory exhibits variations that are generally consistent with the MESSENGER magnetic field observations. Also shown in the figure is the magnetic field topology encountered along the spacecraft trajectory as predicted by the simulation. During the passage through the nightside magnetosphere, field lines with different connectivities are encountered, including closed field lines with both ends connected to the planet seen near closest approach and lobe field lines connected to the solar wind seen during much of the flyby inside the magnetosphere. A direct comparison of the observed field with the model field along the same trajectory is shown in the right-hand side plot of Figure 4. It can be seen that the modeled field is in satisfactory agreement with the observed data. Not only the overall trend but also the variations of the field across different magnetospheric boundaries including the magnetopause, the bow shock and the cross-tail current sheet are all well captured by the MHD model.

3.2. Induction Effect on Mercury's Response to Solar Wind Forcing

The key development of the Mercury MHD model presented here is the capability to self-consistently model the electromagnetic response of the planetary interior to the external forcing. As mentioned earlier, such an attempt has been undertaken by *Janhunen and Kallio* [2004] and *Müller et al.* [2012], both of whom adapted a 3-D hybrid model to Mercury that included the planetary interior with a specified conductivity distribution. *Janhunen and Kallio* [2004] used their model to investigate the role of the surface conductivity in closing magnetospheric currents, the signature of which has recently been identified in MESSENGER magnetic field measurements [*Anderson et al.*, 2014]. The model of *Müller et al.* [2012] has been used to simulate MESSENGER's first flyby and shown to reproduce MESSENGER observations reasonably well. However, the induction effect arising from the core was not clearly demonstrated in the two modeling studies because

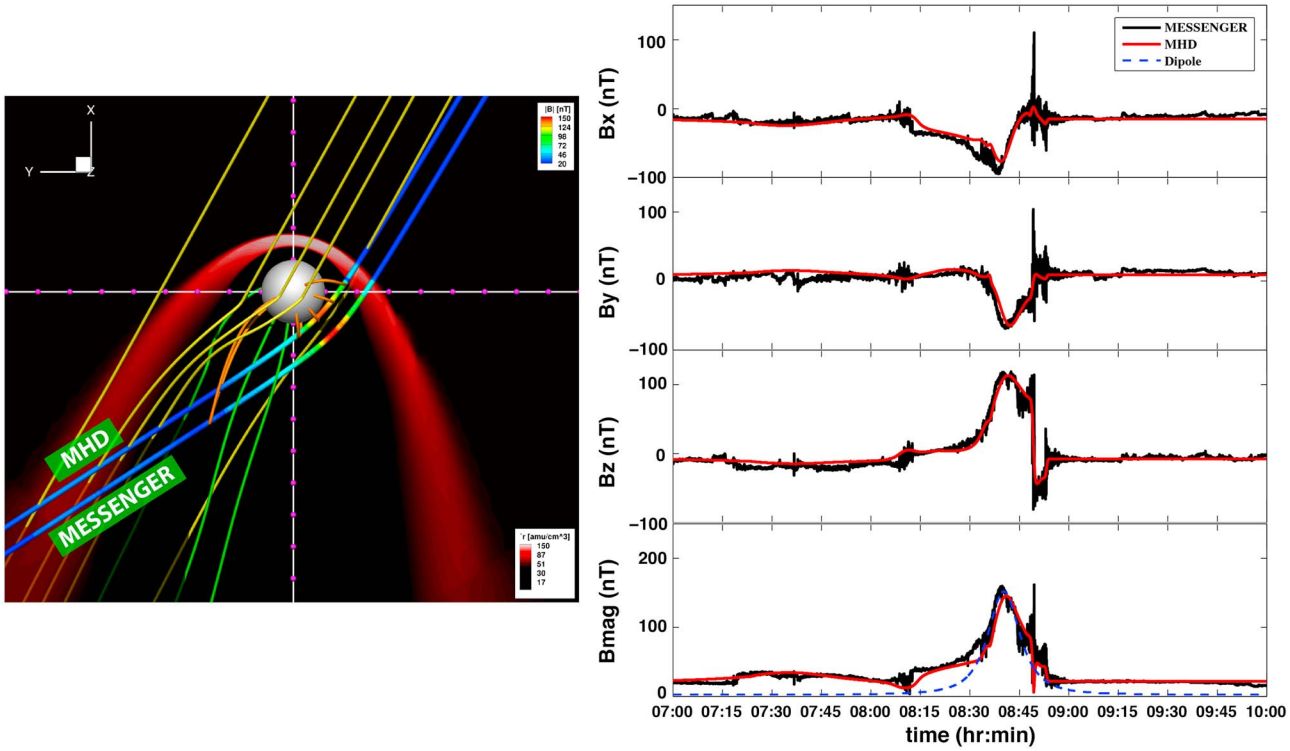

Figure 4. Results from a simulation of the MESSENGER M2 flyby. (left) A perspective of the simulated magnetic field geometry along the flyby trajectory viewed from the north down to the equatorial plane. Color contours of plasma density (according to the bottom right color bar) extracted from the simulation are plotted to show the magnetospheric boundaries. Modeled magnetic field strength is shown as colors (according to the top right color bar) along the original flyby trajectory, while the observed field strength is plotted along a trajectory shifted slightly toward downstream for comparison. Sampled field lines are color coded according to their connectivities: yellow are external field lines, orange represent closed field lines, and green are open field lines with one end on Mercury and the other in the solar wind. (right) Magnetic field comparison between MESSENGER magnetometer data in black and the simulation results in red. The three magnetic components in the MSO coordinate system and the field magnitude are shown. Dashed blue line in the last panel shows the strength of the planetary dipole.

both models employed steady solar wind conditions as input and focused on the steady-state behavior of the magnetosphere, as done with most global models applied to Mercury.

To clearly illustrate how the induction effect is captured by our global MHD model, we have carried out several proof-of-concept time-dependent simulations in which the model is driven by solar wind input that contains different levels of solar wind pressure enhancement. As an example, here we show results from a simulation that is initialized using the solar wind input used for the M2 flyby described above, which has an upstream density of 40 cm^{-3} and a speed of ~ 400 km/s yielding a dynamic pressure of ~ 11 nPa. After the system has reached a quasi steady state from which the model-data comparison shown in Figure 4 was extracted, we introduce a pressure enhancement in the solar wind by increasing the density to 80 cm^{-3} and the speed to 700 km/s in 30 s, yielding a dynamic pressure of ~ 66 nPa that remains fixed thereafter. As will be discussed in section 4, for the conductivity distribution assumed, the inductive response of the interior in our model is almost instantaneous as long as the external variations of interest occur on time scales between $\sim 10^{-2}$ s and a couple of hours. Therefore, while the final state of the compressed magnetosphere depends on the magnitude of pressure change, it would remain virtually the same for different rates of pressure change that fall within the aforementioned range.

Figure 5 shows a comparison of the states of the modeled magnetosphere prior to and after the compression induced by the pressure enhancement. Starting with the magnetospheric state prior to the compression (Figures 5a and 5b), one can readily identify familiar structures present in the magnetosphere. For instance, the dayside magnetopause is characterized by an elongated sheet of current (Chapman-Ferraro current) flowing in the dawn-to-dusk direction ($+J_y$). The Chapman-Ferraro current is closed on the magnetopause by currents that are poleward of the cusps and flowing in the opposite direction ($-J_y$ as shown by the blue color in Figure 5a). An extended cross-tail current sheet exists on the nightside with its inner edge located at

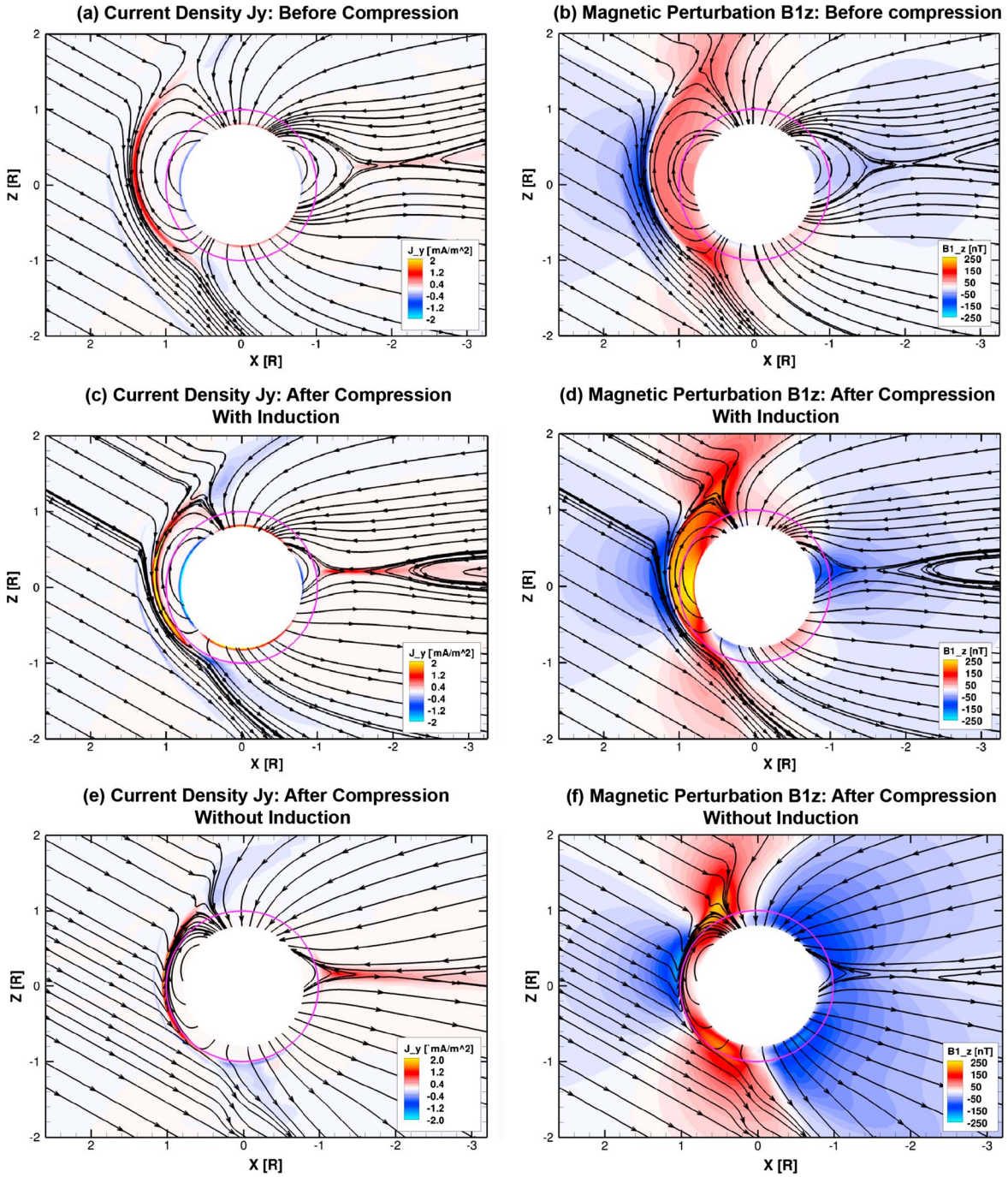

Figure 5. Comparison of the state of the magnetosphere prior to and after the compression induced by a solar wind pressure enhancement. (a and b) Color contours of the *y* component of the current density and the *z* component of magnetic field perturbation (the difference between the total field and the dipole field) overlaid with sampled field lines in the *XZ* plane. The results are for the state prior to compression. (c and d) Same as Figures 5a and 5b but for the state after compression with the induction effect included. (e and f) Same as Figures 5c and 5d but without the induction effect. The magenta circle of radius 1 R_M represents the planetary surface, while the white disk of 0.8 R_M shows the simulation inner boundary.

~1.4 R_M, consistent with that determined from the MESSENGER orbital data [*Johnson et al.*, 2012]. Due to the northward offset of the internal dipole, both the magnetopause and tail current sheets are displaced toward the north. As a result, the magnetopause and hence the current sheet lie closer to the planet in the south than in the north. Figure 5b shows the magnetic field perturbations associated with the external current systems plotted in Figure 5a. In the dayside magnetosphere, the magnetopause current mainly produces positive perturbations in B_z. For the M2 flyby conditions used, which are close to the average conditions at Mercury, the B_z

perturbation at the subsolar surface is ~ 80 nT. Because of the asymmetry of the current system, the magnetic perturbations are also asymmetric around the equator. The peak of the perturbation field strength is shifted toward the south because the magnetopause lies closer to the surface in the southern hemisphere. On the nightside, the negative B_z perturbations arise mainly from the tail current sheet, which is also displaced northward due primarily to the offset dipole. The maximum $|B_z|$ perturbation at the surface is ~ 40 nT. Comparing our model results with the paraboloid magnetospheric model developed by *Alexeev et al.* [2010] and *Johnson et al.* [2012] using MESSENGER data, we find that the characteristics of the magnetic perturbations associated with the external magnetospheric currents in our model, such as the spatial distribution and perturbation strength, are generally consistent with the fitting results of the Johnson et al. baseline model (their Figure 12).

Figures 5c and 5d show the magnetospheric state at ~3 min after the pressure enhancement arrives at the dayside magnetopause. As expected, the enhanced external pressure causes the magnetopause to move closer to the planet, resulting in intensified Chapman-Ferraro currents (Figure 5c). The compression also causes the tail current sheet to intensify and to move closer to the surface. The tail X-line is located at ~$1.5R_M$ in the compressed magnetosphere, closer to the surface compared to that in the pre-compression state. Comparing Figure 5c with Figure 5a, one finds that there are currents flowing near the core-mantle boundary and those currents become stronger in intensity after compression. The sense of the current flows is consistent with that of the induction currents expected to arise in response to external magnetic field changes. In particular, on the dayside, the negative J_y in the equatorial region produces positive B_z perturbations outside the conducting core and negative B_z perturbations inside the core, which act to cancel out the increased positive B_z perturbations arising for the intensified magnetopause current. A similar inductive response also arises on the nightside in response to the changes in the tail current sheet. The negative J_y in the equatorial region produces negative B_z perturbations outside the core and positive B_z perturbations inside, which act to cancel out the increased negative B_z perturbations arising for the enhanced tail current. The intensification of the currents flowing near the conducting core after compression is, therefore, a direct consequence of the induction effect.

The magnetic perturbations shown in Figure 5d basically confirms this picture. The perturbations evidently become stronger in the compressed state due to both the intensified magnetospheric current systems and the induction effect of the core. The peak perturbation field at the surface now reaches ~ 235 nT on the dayside and ~ −120 nT on the nightside, both of which are nearly 3 times the values identified in the precompression state and become comparable to the surface field of the planetary dipole.

As suggested by the previous work [e.g., *Hood and Schubert*, 1979; *Suess and Goldstein*, 1979; *Glassmeier et al.*, 2007a; *Slavin et al.*, 2014], one of the important consequences of the induction effect is its influence on the size of the magnetosphere. In our simulation that includes the induction effect, the magnetopause standoff distance is ~1.15 R_M after the compression induced by an increased solar wind dynamic pressure of 66 nPa. For comparison, we estimate the magnetopause standoff distance for the same solar wind pressure but in the absence of induction. To do so, we turn to a simulation in which the whole planetary interior is treated as a purely resistive body (without a conducting core) and the upstream solar wind pressure is fixed at the same 66 nPa as shown in Figures 5c and 5d such that there is no inductive response arising from the interior. Figures 5e and 5f show a snapshot of the simulation after it has reached a quasi steady state. As expected for the high solar wind pressure imposed, both the magnetopause and tail current sheets move closer to the planet. In contrast to the results shown in Figures 5c and 5d where the standoff distance is ~1.15 R_M, the dayside magnetopause is located at a distance of ~1.04 R_M in the simulation without the induction effect. For the external pressure conditions considered here, an approximately 10% increase in the magnetopause standoff distance is seen in our simulations due to the induction effect alone. Our model results therefore confirm that the induction effect has significant influences on the global configuration of Mercury's magnetosphere, as predicted by the previous theoretical studies.

4. Discussion

At Mercury, the solar wind and IMF conditions change on a variety of temporal scales ranging from seconds associated with high-frequency fluctuations of the IMF [*Korth et al.*, 2011] to hours associated with the passages of coronal mass ejections (CMEs) or high-speed streams. The inductive response of Mercury's interior to the temporal changes in the external conditions depends on the distribution of the interior conductivity as well as the time scales on which the changes occur. In the simulations presented here, which are performed

as proof of concept of the new modeling capability, we used a time-varying solar wind input that contains pressure variations occurring on the order of tens of seconds. It is worthwhile to compare this time scale with the characteristic time scales on which the different regions of the interior respond inductively to external variations. For the conductivity profile adopted in this simulation (Figure 2), which has an average value of $\sim 10^{-7}$ S/m for the mantle, the time it takes for the magnetic field to diffuse through the mantle (from the surface to ~350 km depth) is about 0.02 s, indicating that any external variations occurring on time scales longer than 0.02 s in effect are able to penetrate through the resistive mantle to the core-mantle boundary where the conductivity rapidly increases to values of $\sim 10^5$ S/m in our model. On the other hand, the time for the field to diffuse through the outer layer of the conducting core with a thickness of ~120 km is about 10^4 s (or 2.7 h), implying that external changes on time scales shorter than 2.7 h are not able to penetrate this layer. The pressure enhancement introduced in our simulation shown in section 3.2 occurs within 30 s, which is much longer than the diffusion time through the mantle and much shorter than the diffusion time through the outer layer of the conducting core. Therefore, in this particular case the signal of the compression imposed by the solar wind is able to penetrate fully to the outer layer of the conducting core, where it is able to generate an instantaneous inductive response with almost 100% efficiency due to the high conductivity. There is a wide range of conductivity values estimated for Mercury's mantle [e.g., *Verhoeven et al.*, 2009; *Hauck et al.*, 2013]. With a different conductivity distribution, details of the inductive response would change and need to be determined quantitatively by using a coupled global model like the one presented in this paper. However, we expect that the general behavior of the system will remain qualitatively similar to the results shown here.

As discussed in section 3.2, the magnetospheric configuration is highly asymmetric around the equator due to the large offset of the internal dipole. As a result, the magnetic perturbations associated with the asymmetric magnetospheric current systems not only are spatially nonuniform but also exhibit strong asymmetries in the north-south direction. Therefore, the field induced at the core by the external magnetospheric currents should contain significant power in high-order moments. Quantitative characterization of the induced field and its dependence on the upstream solar wind conditions would require further analysis that we aim to undertake in future work. The asymmetric magnetospheric configuration also has important implications on the extent to which the solar wind particles can have access to the planet's surface, which is of relevance to the generation of Mercury's tenuous exosphere. During periods of high solar wind pressure, while the magnetopause may still stand well above the surface in the northern hemisphere providing a shield for much of the dayside magnetosphere from direct impact of the solar wind particles, the magnetopause may be located very close to or even in contact with the surface at high southern latitudes (Figures 5c and 5d), in which case the southern hemisphere is more susceptible to direct solar wind particle precipitation. An important question related to the solar wind-surface interaction is under what external conditions the solar wind can have direct interaction with the surface. *Kabin et al.* [2000] made the first attempt to address this question by using a global MHD model in which the planet was treated as an absorbing body and thus the induction effect was not included. Their model results suggested that it is possible that the entire dayside magnetosphere may "disappear" under extreme conditions of high solar wind pressure. However, the minimum pressure required in order for the solar wind to compress the dayside magnetosphere down to the surface needs to be reassessed with the induction effect taken into account, a subject that will be investigated in our future work using the MHD model presented here.

As mentioned in section 1, MESSENGER observations clearly indicate that magnetic reconnection is the dominant process that controls the global configuration and dynamics of Mercury's magnetosphere [e.g., *Slavin et al.*, 2009; *Dibraccio et al.*, 2013]. An important consequence of intense reconnection on Mercury's magnetopause is that it can erode the dayside magnetosphere, causing the magnetopause to move closer to the planet [*Slavin and Holzer*, 1979]. The erosion arising from reconnection tends to impose an effect on the dayside magnetosphere that is opposite to that resulting from the induction of the conducting core. It is very likely that Mercury's magnetospheric structure is determined by the two processes together. Indeed, the recent analysis of the impact of extreme solar events on Mercury by *Slavin et al.* [2014] suggests that the induction effect of the core and the erosion of the magnetosphere due to intense reconnection appear to be equally important in determining the large-scale configuration of Mercury's magnetosphere. In the present global MHD model, magnetic reconnection occurs in a way facilitated by numerical diffusion. Although the global coupling efficiency between the solar wind and the magnetosphere through reconnection appears to be in a reasonably good agreement with that inferred from in situ observations as discussed in section 3.1, future modeling efforts need to be devoted to improving the way in which reconnection is handled in global

simulations through elaborate approaches, such as including the Hall physics [*Tóth et al.*, 2008] or using an embedded particle-in-cell code [*Daldorff et al.*, 2014], in order to more realistically characterize the effect of reconnection on the global magnetosphere.

5. Summary and Conclusions

We have developed a Mercury global MHD model that electromagnetically couples the planetary interior composed of layers of different electrical conductivities to the surrounding magnetosphere in order to self-consistently characterize Mercury's inductive response to time-varying external conditions, such as those during CME impacts [*Slavin et al.*, 2014]. To verify the feasibility of the coupling approach implemented in the global model, we have performed simulations using nominal external solar wind conditions observed at Mercury's orbit and internal conditions appropriate for Mercury. Specifically, a northward offset dipole is used to represent Mercury's planetary field and the planetary interior is modeled as a spherical body consisting of a highly resistive mantle and a highly conducting core of radius of 0.8 R_M.

Our model results indicate that Mercury's magnetosphere exhibits strong asymmetries with respect to the planetary equator due to the northward offset of the internal dipole. As a result, the magnetospheric current systems, including both the magnetopause and tail currents, also display significant asymmetries. Comparison of our model results with available MESSENGER observations shows that the model is able to provide a reasonably good description of the large-scale structure of Mercury's magnetosphere. In particular, the location and shape of the magnetopause boundary are consistent with the empirical model developed based on MESSENGER observations [*Winslow et al.*, 2013]. Other important features of the magnetosphere, such as the location of tail X-line and the cross-polar cap potential drop, are also in general agreement with those inferred from MESSENGER in situ observations under nominal conditions [*Slavin et al.*, 2009; *Dibraccio et al.*, 2014]. As a further validation of the model, the modeled magnetic field is compared with the observed field for the MESSENGER's second flyby, which also yields a satisfactory agreement.

To demonstrate the capability of our new model in capturing the induction effect, we have carried out idealized time-dependent simulations in which Mercury's magnetosphere is impacted by solar wind pressure enhancement. Our results show that the solar wind compression causes both the magnetopause and tail current sheets to intensify and move closer to the planet. As a consequence, the magnetic perturbations associated with the external current systems are enhanced throughout much of the magnetosphere and the external perturbations are able to propagate inward through the resistive mantle and reach the outer layer of the conducting core, where intense electric currents are induced that flow in a sense to prevent the external perturbations from penetrating into the core. Comparing the states of the magnetosphere prior to and after the compression, we find that because of the induction effect, Mercury's core can impose strong global influences on the way Mercury responds to changes in the external environment, including modifying the global magnetospheric structure and affecting the extent to which the solar wind directly impacts the planetary surface. Our model results show that the asymmetric external current systems produce an inducing field that is spatially nonuniform and asymmetric in nature, suggesting that the induced field should contain significant power in high-order moments, an important feature that calls for further quantitative analysis. The global model shown here represents a crucial step toward establishing a modeling framework that enables self-consistent, quantitative characterization of the tightly coupled planetary interior-magnetosphere at Mercury.

Acknowledgments

This work is supported by the NASA Solar System Workings program through grant NNX15AH28G and the Heliophysics Supporting Research program through grant NNX15AJ68G. The MESSENGER project is supported by the NASA Discovery Program under contracts NASW-00002 to the Carnegie Institution of Washington and NAS5-97271 to the Johns Hopkins University Applied Physics Laboratory. The MESSENGER data used in this study were downloaded from the PPI node of the Planetary Data System (http://ppi.pds.nasa.gov), and the model data were obtained from simulations using the SWMF/BATSRUS code developed at the University of Michigan, which is available at http://csem.engin.umich.edu/tools/swmf/. The simulation runs were performed on the Pleiades supercomputer managed by the NASA Advanced Supercomputing (NAS) division.

Yuming Wang thanks David Schriver and one anonymous reviewer for their assistance in evaluating this paper.

References

Alexeev, I. I., et al. (2010), Mercury's magnetospheric magnetic field after the first two MESSENGER flybys, *Icarus*, *209*, 23–39, doi:10.1016/j.icarus.2010.01.024.

Anderson, B. J., C. L. Johnson, H. Korth, M. E. Purucker, R. M. Winslow, J. A. Slavin, S. C. Solomon, R. L. McNutt, J. M. Raines, and T. H. Zurbuchen (2011), The global magnetic field of Mercury from MESSENGER orbital observations, *Science*, *333*, 1859–1862, doi:10.1126/science.1211001.

Anderson, B. J., C. L. Johnson, H. Korth, J. A. Slavin, R. M. Winslow, R. J. Phillips, R. L. McNutt, and S. C. Solomon (2014), Steady-state field-aligned currents at Mercury, *Geophys. Res. Lett.*, *41*, 7444–7452, doi:10.1002/2014GL061677.

Baker, D. N., et al. (2013), Solar wind forcing at Mercury: WSA-ENLIL model results, *J. Geophys. Res. Space. Physics*, *118*, 45–57, doi:10.1029/2012JA018064.

Benna, M., et al. (2010), Modeling of the magnetosphere of Mercury at the time of the first MESSENGER flyby, *Icarus*, *209*, 3–10, doi:10.1016/j.icarus.2009.11.036.

Daldorff, L. K. S., G. Tóth, T. I. Gombosi, G. Lapenta, J. Amaya, S. Markidis, and J. U. Brackbill (2014), Two-way coupling of a global Hall magnetohydrodynamics model with a local implicit particle-in-cell model, *J. Comput. Phys.*, *268*, 236–254, doi:10.1016/j.jcp.2014.03.009.

Dibraccio, G. A., J. A. Slavin, S. A. Boardsen, B. J. Anderson, H. Korth, T. H. Zurbuchen, J. M. Raines, D. N. Baker, R. L. McNutt, and S. C. Solomon (2013), MESSENGER observations of magnetopause structure and dynamics at Mercury, *J. Geophys. Res. Space Physics*, *118*, 997–1008, doi:10.1002/jgra.50123.

Dibraccio, G. A., et al. (2014), MESSENGER oobservations of flux ropes in Mercury's magnetotail, *Planet. Space Sci.*, doi:10.1016/j.pss.2014.12.016.

Glassmeier, K.-H., J. Grosser, U. Auster, D. Constantinescu, Y. Narita, and S. Stellmach (2007a), Electromagnetic induction effects and dynamo action in the Hermean system, *Space Sci. Rev.*, *132*, 511–527, doi:10.1007/s11214-007-9244-9.

Glassmeier, K.-H., H.-U. Auster, and U. Motschmann (2007b), A feedback dynamo generating Mercury's magnetic field, *Geophys. Res. Lett.*, *34*, L22201, doi:10.1029/2007GL031662.

Gombosi, T. I., G. Tóth, D. L. De Zeeuw, K. C. Hansen, K. Kabin, and K. G. Powell (2002), Semi-relativistic magnetohydrodynamics and physics-based convergence acceleration, *J. Comput. Phys.*, *177*, 176–205, doi:10.1006/jcph.2002.7009.

Hauck, S. A., et al. (2013), The curious case of Mercury's internal structure, *J. Geophys. Res. Planets*, *118*, 1204–1220, doi:10.1002/jgre.20091.

Heyner, D., J. Wicht, N. Gómez-Pérez, D. Schmitt, H.-U. Auster, and K.-H. Glassmeier (2011), Evidence from numerical experiments for a feedback dynamo generating Mercury's magnetic field, *Science*, *334*, 1690–1693, doi:10.1126/science.1207290.

Hood, L., and G. Schubert (1979), Inhibition of solar wind impingement on Mercury by planetary induction currents, *J. Geophys. Res.*, *84*, 2641–2647, doi:10.1029/JA084iA06p02641.

Imber, S. M., J. A. Slavin, S. A. Boardsen, B. J. Anderson, H. Korth, R. L. McNutt, and S. C. Solomon (2014), MESSENGER observations of large dayside flux transfer events: Do they drive Mercury's substorm cycle?, *J. Geophys. Res. Space Physics*, *119*, 5613–5623, doi:10.1002/2014JA019884.

Ip, W.-H., and A. Kopp (2002), MHD simulations of the solar wind interaction with Mercury, *J. Geophys. Res.*, *107*(A11), 1348, doi:10.1029/2001JA009171.

Janhunen, P., and E. Kallio (2004), Surface conductivity of Mercury provides current closure and may affect magnetospheric symmetry, *Ann. Geophys.*, *22*, 1829–1837, doi:10.5194/angeo-22-1829-2004.

Jia, X., R. J. Walker, M. G. Kivelson, K. K. Khurana, and J. A. Linker (2008), Three-dimensional MHD simulations of Ganymede's magnetosphere, *J. Geophys. Res.*, *113*, A06212, doi:10.1029/2007JA012748.

Jia, X., R. J. Walker, M. G. Kivelson, K. K. Khurana, and J. A. Linker (2009), Properties of Ganymede's magnetosphere inferred from improved three-dimensional MHD simulations, *J. Geophys. Res.*, *114*, A09209, doi:10.1029/2009JA014375.

Jia, X., R. J. Walker, M. G. Kivelson, K. K. Khurana, and J. A. Linker (2010), Dynamics of Ganymede's magnetopause: Intermittent reconnection under steady external conditions, *J. Geophys. Res.*, *115*, A12202, doi:10.1029/2010JA015771.

Johnson, C. L., et al. (2012), MESSENGER observations of Mercury's magnetic field structure, *J. Geophys. Res.*, *117*, E00L14, doi:10.1029/2012JE004217.

Kabin, K., T. I. Gombosi, D. L. DeZeeuw, and K. G. Powell (2000), Interaction of Mercury with the solar wind, *Icarus*, *143*, 397–406, doi:10.1006/icar.1999.6252.

Kabin, K., M. H. Heimpel, R. Rankin, J. M. Aurnou, N. Gómez-Pérez, J. Paral, T. I. Gombosi, T. H. Zurbuchen, P. L. Koehn, and D. L. DeZeeuw (2008), Global MHD modeling of Mercury's magnetosphere with applications to the MESSENGER mission and dynamo theory, *Icarus*, *195*, 1–15, doi:10.1016/j.icarus.2007.11.028.

Kallio, E., and P. Janhunen (2003), Modelling the solar wind interaction with Mercury by a quasi-neutral hybrid model, *Ann. Geophys.*, *21*, 2133–2145, doi:10.5194/angeo-21-2133-2003.

Khurana, K. K., X. Jia, M. G. Kivelson, F. Nimmo, G. Schubert, and C. T. Russell (2011), Evidence of a global magma ocean in Io's interior, *Science*, *332*, 1186–1189, doi:10.1126/science.1201425.

Kidder, A., R. M. Winglee, and E. M. Harnett (2008), Erosion of the dayside magnetosphere at Mercury in association with ion outflows and flux rope generation, *J. Geophys. Res.*, *113*, A09223, doi:10.1029/2008JA013038.

Korth, H., B. J. Anderson, T. H. Zurbuchen, J. A. Slavin, S. Perri, S. A. Boardsen, D. N. Baker, S. C. Solomon, and R. L. McNutt (2011), The interplanetary magnetic field environment at Mercury's orbit, *Planet. Space Sci.*, *59*, 2075–2085, doi:10.1016/j.pss.2010.10.014.

Linker, J. A., K. K. Khurana, M. G. Kivelson, and R. J. Walker (1998), MHD simulations of Io's interaction with the plasma torus, *J. Geophys. Res.*, *103*(E9), 19,867–19,877.

Müller, J., S. Simon, Y.-C. Wang, U. Motschmann, D. Heyner, J. Schüle, W.-H. Ip, G. Kleindienst, and G. J. Pringle (2012), Origin of Mercury's double magnetopause: 3D hybrid simulation study with A.I.K.E.F., *Icarus*, *218*, 666–687, doi:10.1016/j.icarus.2011.12.028.

Powell, K. G., P. L. Roe, T. J. Linde, T. I. Gombosi, and D. L. D. Zeeuw (1999), A solution-adaptive upwind scheme for ideal magnetohydrodynamics, *J. Comput. Phys.*, *154*, 284–309.

Raines, J. M., D. J. Gershman, J. A. Slavin, T. H. Zurbuchen, H. Korth, B. J. Anderson, and S. C. Solomon (2014), Structure and dynamics of Mercury's magnetospheric cusp: MESSENGER measurements of protons and planetary ions, *J. Geophys. Res. Space Physics*, *119*, 6587–6602, doi:10.1002/2014JA020120.

Richer, E., R. Modolo, G. M. Chanteur, S. Hess, and F. Leblanc (2012), A global hybrid model for Mercury's interaction with the solar wind: Case study of the dipole representation, *J. Geophys. Res.*, *117*, A10228, doi:10.1029/2012JA017898.

Siegfried, R. W., II, and S. C. Solomon (1974), Mercury—Internal structure and thermal evolution, *Icarus*, *23*, 192–205, doi:10.1016/0019-1035(74)90005-0.

Slavin, J. A., and R. E. Holzer (1979), The effect of erosion on the solar wind stand-off distance at Mercury, *J. Geophys. Res.*, *84*, 2076–2082, doi:10.1029/JA084iA05p02076.

Slavin, J. A., et al. (2009), MESSENGER observations of magnetic reconnection in Mercury's magnetosphere, *Science*, *324*, 606–610, doi:10.1126/science.1172011.

Slavin, J. A., et al. (2010), MESSENGER observations of extreme loading and unloading of Mercury's magnetic tail, *Science*, *329*, 665–668, doi:10.1126/science.1188067.

Slavin, J. A., et al. (2012), MESSENGER observations of a flux-transfer-event shower at Mercury, *J. Geophys. Res.*, *117*, A00M06, doi:10.1029/2012JA017926.

Slavin, J. A., et al. (2014), MESSENGER observations of Mercury's magnetosphere under extreme solar wind conditions, *J. Geophys. Res. Space Physics*, *119*, 8087–8116, doi:10.1002/2014JA020319.

Smith, D. E., et al. (2012), Gravity field and internal structure of Mercury from MESSENGER, *Science*, *336*, 214–217, doi:10.1126/science.1218809.

Suess, S. T., and B. E. Goldstein (1979), Compression of the Hermaean magnetosphere by the solar wind, *J. Geophys. Res.*, *84*, 3306–3312, doi:10.1029/JA084iA07p03306.

Sundberg, T., et al. (2012), MESSENGER observations of dipolarization events in Mercury's magnetotail, *J. Geophys. Res.*, *117*, A00M03, doi:10.1029/2012JA017756.

Tóth, G., Y. Ma, and T. I. Gombosi (2008), Hall magnetohydrodynamics on block-adaptive grids, *J. Comput. Phys.*, *227*, 6967–6984, doi:10.1016/j.jcp.2008.04.010.

Tóth, G., et al. (2012), Adaptive numerical algorithms in space weather modeling, *J. Comput. Phys.*, *231*, 870–903, doi:10.1016/j.jcp.2011.02.006.

Trávníček, P., P. Hellinger, and D. Schriver (2007), Structure of Mercury's magnetosphere for different pressure of the solar wind: Three dimensional hybrid simulations, *Geophys. Res. Lett.*, *34*, L05104, doi:10.1029/2006GL028518.

Verhoeven, O., P. Tarits, P. Vacher, A. Rivoldini, and T. Van Hoolst (2009), Composition and formation of Mercury: Constraints from future electrical conductivity measurements, *Planet. Space Sci.*, *57*, 296–305, doi:10.1016/j.pss.2008.11.015.

Wang, Y.-C., J. Mueller, U. Motschmann, and W.-H. Ip (2010), A hybrid simulation of Mercury's magnetosphere for the MESSENGER encounters in year 2008, *Icarus*, *209*, 46–52, doi:10.1016/j.icarus.2010.05.020.

Winslow, R. M., C. L. Johnson, B. J. Anderson, H. Korth, J. A. Slavin, M. E. Purucker, and S. C. Solomon (2012), Observations of Mercury's northern cusp region with MESSENGER's magnetometer, *Geophys. Res. Lett.*, *39*, L08112, doi:10.1029/2012GL051472.

Winslow, R. M., B. J. Anderson, C. L. Johnson, J. A. Slavin, H. Korth, M. E. Purucker, D. N. Baker, and S. C. Solomon (2013), Mercury's magnetopause and bow shock from MESSENGER magnetometer observations, *J. Geophys. Res. Space Physics*, *118*, 2213–2227, doi:10.1002/jgra.50237.

Zurbuchen, T. H., J. M. Raines, G. Gloeckler, S. M. Krimigis, J. A. Slavin, P. L. Koehn, R. M. Killen, A. L. Sprague, R. L. McNutt, and S. C. Solomon (2008), MESSENGER observations of the composition of Mercury's ionized exosphere and plasma environment, *Science*, *321*, 90–92, doi:10.1126/science.1159314.

Zurbuchen, T. H., et al. (2011), MESSENGER observations of the spatial distribution of planetary ions near Mercury, *Science*, *333*, 1862–1865, doi:10.1126/science.1211302.